In Situ Activated Co$_{3-x}$Ni$_x$O$_4$ as a Highly Active and Ultrastable Electrocatalyst for Hydrogen Generation

Kailu Guo

Yantao Wang

Junfeng Huang

Min Lu

Hua Li

See next page for additional authors

Authors

Kailu Guo, Yantao Wang, Junfeng Huang, Min Lu, Hua Li, Yong Peng, Pinxian Xi, Haoli Zhang, Jier Huang, Siyu Lu, and Cailing Xu

In Situ Activated Co$_{3-x}$Ni$_x$O$_4$ as a Highly Active and Ultrastable Electrocatalyst for Hydrogen Generation

Kailu Guo
State Key Laboratory of Applied Organic Chemistry, Laboratory of Special Function Materials and Structure Design of the Ministry of Education, College of Chemistry and Chemical Engineering, Lanzhou University, Lanzhou 730000, People's Republic of China

Yantao Wang
State Key Laboratory of Applied Organic Chemistry, Laboratory of Special Function Materials and Structure Design of the Ministry of Education, College of Chemistry and Chemical Engineering, Lanzho University, Lanzhou 730000, People's Republic of China

Junfeng Huang,
State Key Laboratory of Applied Organic Chemistry, Laboratory of Special Function Materials and Structure Design of the Ministry of Education, College of Chemistry and Chemical Engineering, Lanzho University, Lanzhou 730000, People's Republic of China

Min Lu

State Key Laboratory of Applied Organic Chemistry, Laboratory of Special Function Materials and Structure Design of the Ministry of Education, College of Chemistry and Chemical Engineering, Lanzho University, Lanzhou 730000, People's Republic of China

Hua Li

Key Laboratory of Magnetism and Magnetic Materials of Ministry of Education, School of Physical Science and Technology, Lanzhou University, Lanzhou 730000, People's Republic of China

Yong Peng,

Key Laboratory of Magnetism and Magnetic Materials of Ministry of Education, School of Physical Science and Technology, Lanzhou University, Lanzhou 730000, People's Republic of China

Pinxian Xi

State Key Laboratory of Applied Organic Chemistry, Laboratory of Special Function Materials and Structure Design of the Ministry of Education, College of Chemistry and Chemical Engineering, Lanzho University, Lanzhou 730000, People's Republic of China

Haoli Zhang

State Key Laboratory of Applied Organic Chemistry, Laboratory of Special Function Materials and Structure Design of the Ministry of Education, College of Chemistry and Chemical Engineering, Lanzho University, Lanzhou 730000, People's Republic of China

Jier Huang

Department of Chemistry, Marquette University, Milwaukee Wisconsin

Siyu Lu

Green Catalysis Center and College of Chemistry, Zhengzhou University, Zhengzhou 450000, People's Republic of China

Cailing Xu*

State Key Laboratory of Applied Organic Chemistry, Laboratory of Special Function Materials and Structure Design of the Ministry of Education, College of Chemistry and Chemical Engineering, Lanzhou University, Lanzhou 730000, People's Republic of China

Abstract
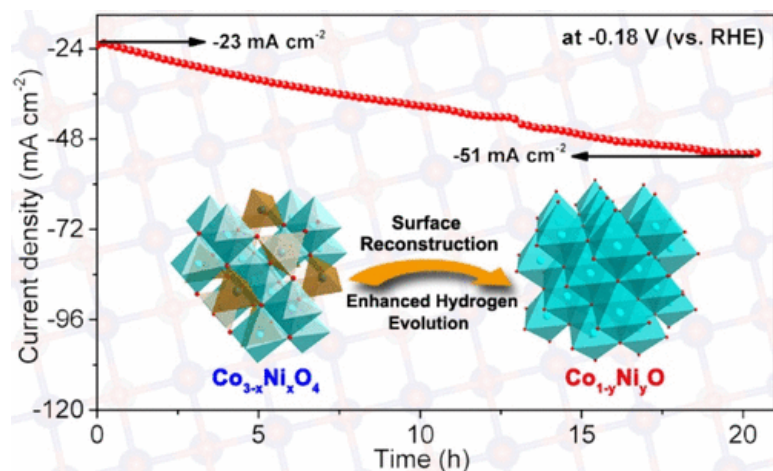
The spinel Co_3O_4 has emerged as a promising alternative to noble-metal-based electrocatalysts for electrochemical water electrolysis in alkaline medium. However, pure Co_3O_4, despite having high activity in

anodic water oxidation, remains inactive toward the hydrogen evolution reaction (HER). Here, a Ni-doped $Co_3O_4(Co_{3-x}Ni_xO_4)$ prepared by a simple method exhibits favorable HER activity and stability (>300 h, whether in 1 M KOH or the realistic 30 wt % KOH solution) after *in situ* electrochemical activation, outperforming almost all of the oxide-based electrocatalysts. More importantly, using the combination of *in situ* Raman spectroscopy and multiple high-resolution electron microscopy techniques, it is identified that the surface of $Co_{3-x}Ni_xO_4$ crystals is reduced into intertwined $Co_yNi_{1-y}O$ nanoparticles with highly exposed {110} reactive planes. Density functional theory calculations further prove that the Ni-doped CoO component in $Co_yNi_{1-y}O$ plays a major role during the alkaline HER, because the introduction of Ni atoms into Co–O octahedra can optimize the electrical conductivity and tailor the adsorption/desorption free energies of H_{ad} and OH_{ad} intermediates.

KEYWORDS:

Electrocatalyst, electrochemical activation, $Co_yNi_{1-y}O$, $Co_{3-x}Ni_xO_4$, hydrogen evolution reaction

Introduction

Electrochemical water electrolysis to produce hydrogen (H_2) represents one of the best solutions to address the increasing energy crisis and greenhouse effect caused by fossil fuels. (1) To increase the reaction rate and reduce the overpotential of the hydrogen evolution reaction (HER), an electrocatalyst that meets both the technical and economical requirements is required. (2) Among the various catalytic systems that have been reported to date, Pt-based materials are state of the art electrocatalysts for electrocatalytic HER. (3,4) However, the large-scale application of Pt-based catalysts is severely hindered by low element abundance and high cost of Pt. (5,6)

In response to this challenge, great efforts have been devoted to developing catalysts based on earth-abundant metals. (7−14) Among the various catalysts that have been employed, the spinel Co_3O_4 has attracted increasing interest as a water electrolysis catalyst because of its low price, nontoxicity, variable chemical states, and good resistance to alkaline corrosion. (15,16) However, it has been found that pure Co_3O_4, although it displays high activity in anodic water oxidation, (17,18) is inactive toward the HER, which can be attributed to the poor electrical conductivity, inappropriate hydrogen adsorption ability, and limited catalytically active sites. To address these problems, strategies such as doping, oxygen-vacancy engineering, morphology engineering, and heterostructure engineering have been used to optimize the activity of Co_3O_4 for the HER. (17−22) While these efforts have made some progress in improving the catalytic activity, there are still many challenges in employing Co_3O_4-based electrocatalysts for practical H_2 production, among which the poor long-term operational stability is often ignored and needs to be improved. Most of the recently developed HER electrocatalysts can only remain stable for several tens of hours at small current densities, and very few can last for several hundreds of hours. The deactivation can be caused by various adverse microstructural evolutions and the shedding of active species from the current collector during the HER, especially at large current densities. (23,24) In addition, endeavors toward uncovering the catalytically active species responsible for the HER activity have been limited. This is because these prior studies assumed that the original structure of Co_3O_4 is the catalytically active species for the HER, while most catalysts indeed undergo a structural self-reconstruction or phase transition process in the reductive environment. (25,26) For instance, a Ni-thiolate coordination polymer could be reduced *in situ* into Ni metal during the HER in alkaline solution, which acted as the real active site for hydrogen generation. (27) Similarly, during electrochemical HER testing, core@shell iron@iron oxysulfide nanoparticles as the catalytically active phase are generated *in situ* on FeS nanosheets. (28) Therefore, developing highly active and ultrastable Co_3O_4-based electrocatalysts and unraveling the actual active species during the HER still remain a significant challenge.

In this work, we report a Ni-doped spinel Co_3O_4 (denoted $Co_{3-x}Ni_xO_4$) crystal deposited on Ni foam (NF) as a highly efficient and robust HER electrocatalyst with an overpotential of 57 mV at −10 mA cm^{-2} and >300 h

durability under alkaline conditions, which surpass almost all of the reported oxide-based electrocatalysts. Employing the techniques of high-resolution electron microscopy and *in situ* Raman spectroscopy, we show that the surface of $Co_{3-x}Ni_xO_4$ crystals is entirely reduced into intertwined $Co_yNi_{1-y}O$ nanoparticles exposing reactive {110} facets after an electrochemical activation. Density functional theory (DFT) calculations further demonstrate that the Ni-doped CoO component in $Co_yNi_{1-y}O$ can acquire good electrical conductivity and appropriate adsorption/desorption free energies of H_{ad} and OH_{ad} intermediates, thus serving as the key active species for the alkaline HER. This work not only demonstrates the capability to significantly improve the HER performance of spinel Co_3O_4 but also provides direct evidence of the catalytically active sites for the HER process.

Results and Discussion

The $Co_{3-x}Ni_xO_4$ crystals were fabricated on NF by a facile one-step hydrothermal method, where NF is used as both the Ni source and substrate (Figure 1a). A plausible formation mechanism of the $Co_{3-x}Ni_xO_4$ crystals is proposed as shown in the Supporting Information. From the X-ray diffraction (XRD) pattern of the obtained sample, seven well-defined diffraction peaks are observed at 19.5, 31.6, 37.2, 38.7, 55.8, 59.6 and 65.2°, except for three typical peaks of the Ni substrate, which can be well indexed to the (111), (220), (311), (222), (422), (511), and (440) planes of the spinel Co_3O_4 (JCPDS 42-1467), respectively (Figure 1b). A scanning electron microscopy (SEM) image shows that the NF skeleton is fully covered by the polyhedral crystals, forming a three-dimensional hierarchical porous structure (Figure 1c). Time-dependent experiments were further carried out to understand the morphology evolution of the $Co_{3-x}Ni_xO_4$ polyhedron, as illustrated in Figure S1. A transmission electron microscopy (TEM) image of $Co_{3-x}Ni_xO_4$ crystals shows polyhedral particles with a diameter of several micrometers and smooth surface (Figure S2a). The lattice fringes with spacings of 2.43 and 2.03 Å correspond to the (311) and (400) crystallographic planes of Co_3O_4, respectively (Figure S2b). An energy dispersive X-ray spectroscopy (EDS) analysis reveals that the Ni:Co:O ratio of the product is 10.01:39.62:50.37 (Figure S2c). Moreover, the corresponding EDS elemental mapping images indicate the homogeneous distribution of Ni, Co, and O elements in the polyhedral particles (Figure 1d–g).
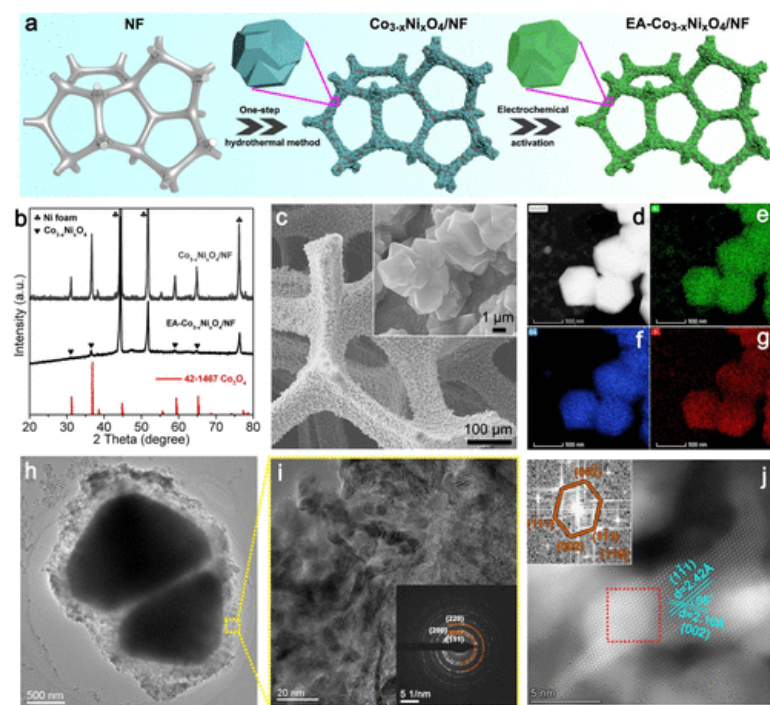
Figure 1. (a) Schematic illustration for the synthesis and *in situ* activation of $Co_{3-x}Ni_xO_4$/NF. (b) XRD patterns of $Co_{3-x}Ni_xO_4$/NF and EA-$Co_{3-x}Ni_xO_4$/NF. (c) SEM image of $Co_{3-x}Ni_xO_4$/NF. (d–g) EDS elemental mapping images of

Co$_{3-x}$Ni$_x$O$_4$ particles detached from NF. (h) TEM image of an EA-Co$_{3-x}$Ni$_x$O$_4$ particle. (i) HRTEM and (j) atomic-scale STEM images of EA-Co$_{3-x}$Ni$_x$O$_4$. The inset in (i) shows the corresponding SAED pattern, and the inset in (j) shows the FFT pattern corresponding to the red dotted area.

The obtained Co$_{3-x}$Ni$_x$O$_4$ crystal is activated *in situ* by a chronoamperometry method in 1 M KOH at room temperature (denoted EA-Co$_{3-x}$Ni$_x$O$_4$), during which the current density gradually increases from −23 to −51 mA cm^{-2} and remains stable after 20 h (Figure S3). The XRD patterns in Figure 1b reveal that, in comparison to those of pristine Co$_{3-x}$Ni$_x$O$_4$, the diffraction peaks of Co$_{3-x}$Ni$_x$O$_4$ in EA-Co$_{3-x}$Ni$_x$O$_4$ are weakening due to a decrease in crystallinity or partial damage of the crystal structure. (29) SEM images show that EA-Co$_{3-x}$Ni$_x$O$_4$ inherits the original polyhedral morphology, and no apparent fracture or shedding is found on the NF surface (Figure S4), implying the good adhesion between EA-Co$_{3-x}$Ni$_x$O$_4$ and the NF substrate. However, a TEM image of EA-Co$_{3-x}$Ni$_x$O$_4$ shows the loose surface structure (Figure 1h), which consists of numerous irregular-shaped particles with a grain size of ∼10–20 nm (Figure 1i). The corresponding selected area electron diffraction (SAED, inset in Figure 1i) further demonstrates that the surface structure of EA-Co$_{3-x}$Ni$_x$O$_4$ has a polycrystalline nature. Interestingly, the bright rings from the inside to the outside can be indexed to the {111}, {200}, and {220} planes of the cubic NiO and/or CoO, indicating the surface structure of Co$_{3-x}$Ni$_x$O$_4$ underwent a transformation from a spinel (Co$_3$O$_4$) to rock salt (CoO). The atomic-scale scanning transmission electron microscopy (STEM) image of the edge of the EA-Co$_{3-x}$Ni$_x$O$_4$ polyhedron displays interplanar distances of 2.42 and 2.10 Å with a characteristic angle of ∼55°, which can be assigned to the (1−11) and (002) planes of cubic NiO (JCPDS 65-2901) or CoO (JCPDS 65-2902), respectively (Figure 1j). The corresponding fast Fourier transform (FFT) pattern (inset in Figure 1j) further reveals the existence of (1−11) and (002) lattice planes. The results indicate that the normal direction to the dominantly exposed crystal planes is the [110] axis, and the geometry of NiO and/or CoO crystallites is likely hexagonal with dominant {110} facets. Previous studies have shown that NiO nanocrystals which expose a high proportion of {110} facets with high surface energy can achieve more efficient water-splitting catalytic performance. (30,31)

In order to further investigate the microstructure and compositional distribution of the nanocrystals on EA-Co$_{3-x}$Ni$_x$O$_4$ surface, we performed high-resolution chemical imaging via STEM-electron energy loss spectroscopy (EELS) mapping (Figure 2a). The results depict that the distribution of O is high even through the analyzed area, whereas the Ni and Co elements show a clear contrast difference in different areas. Nevertheless, from the EELS spectra collected at the nine spots (Figure 2b), it can be observed that a Co (or Ni) signal can be detected even in the area where Ni (or Co) is concentrated. In summary, microscopic-level STEM-EELS mapping combined with atomic-scale STEM analysis unambiguously demonstrates that the surface of the EA-Co$_{3-x}$Ni$_x$O$_4$ polyhedron is composed of {110}-exposed Ni-doped CoO and Co-doped NiO (denoted Co$_y$Ni$_{1-y}$O), which are symbiotic and are intertwined together. Then, the surface valence and microstructure information on EA-Co$_{3-x}$Ni$_x$O$_4$ were investigated by X-ray photoelectron spectroscopy (XPS). As shown in Figure 2c, the Co 2p spectrum of Co$_{3-x}$Ni$_x$O$_4$ exhibits two spin–orbit peaks (Co 2p$_{1/2}$ and Co 2p$_{3/2}$), and the Co 2p$_{3/2}$ peak can be fitted to Co^{3+} (779.3 eV) and Co^{2+} (780.6 eV) peaks together with a satellite peak (784.5 eV). (32) The Co 2p$_{3/2}$ binding energy of EA-Co$_{3-x}$Ni$_x$O$_4$ shows a positive shift by 0.7 eV in comparison with that in Co$_{3-x}$Ni$_x$O$_4$, implying a low electron density. Additionally, it can be clearly observed that the Co^{3+}:Co^{2+} atomic ratio on the surface of EA-Co$_{3-x}$Ni$_x$O$_4$ is higher than that of Co$_{3-x}$Ni$_x$O$_4$. For the Ni 2p spectra, Ni^{2+} signals at 853.6 and 871.7 eV, Ni^{3+} signals at 855.5 and 873.5 eV, and the shakeup satellite peaks at 879.2 and 860.9 eV are clearly observed in both samples (Figure 2d). (33) Note that the Ni^{3+}:Ni^{2+} ratio calculated from the fitted Ni 2p XPS spectra increases from 1.65 to 2.62 after the electrochemical activation. As proven for many analogues, (34,30) when the particle size of Co$_{1-y}$Ni$_y$O is decreased to the nanoscale, surface Ni^{2+}/Co^{2+} atoms are easily oxidized to Ni^{3+}/Co^{3+} due to the high surface energy and rich atomic-scale defects. The O 1s spectrum of Co$_{3-x}$Ni$_x$O$_4$ is clearly deconvoluted into three peaks at around 529.2, 530.8, and 532.6 eV, which can be assigned to the metal–O (O1), −OH groups (O2), and

adsorbed water molecules (O3), respectively (Figure 2e). (35) In comparison to that of $Co_{3-x}Ni_xO_4$, the O2 peak of EA-$Co_{3-x}Ni_xO_4$/NF is shifted to higher energy by ~0.4 eV, and the percentage of O2 content increases from 35.0% to 66.8%, which implies abundant low-coordinated oxygen ions on the surface of EA-$Co_{3-x}Ni_xO_4$. (36,37)
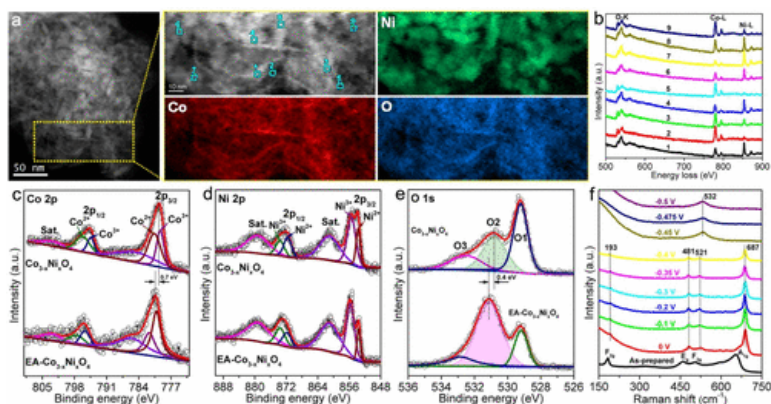
Figure 2. (a) HAADF-STEM image of EA-$Co_{3-x}Ni_xO_4$ and the corresponding EELS elemental maps. (b) EELS spectra of the corresponding regions in (a). High-resolution XPS spectra of (c) Co 2p, (d) Ni 2p, and (e) O 1s. (f) Operando Raman spectra of $Co_{3-x}Ni_xO_4$/NF at various potentials.

In order to further explore the underlying phase evolution of $Co_{3-x}Ni_xO_4$, potential-dependent *operando* Raman spectroscopy was employed to monitor the surface structure evolution during the reduction process (Figure 2f). The Raman spectrum of pristine $Co_{3-x}Ni_xO_4$ shows the characteristic peaks of F_{2g}, E_g, F_{2g}, and A_{1g} modes at 182, 460, 503, and 655 cm^{-1}, respectively. (38,39) As the $Co_{3-x}Ni_xO_4$/NF electrode is immersed into KOH electrolyte (0 V vs RHE), the changes in Raman shift, peak intensity and width are due to the differences between *in situ* and *ex situ* Raman test conditions. (26,38) With an increase in the potential (−0.1 to −0.35 V, vs RHE), the peak intensities at 193, 481, 521, and 687 cm^{-1} gradually decreased, which can be attributed to the gradual decomposition of $Co_{3-x}Ni_xO_4$ under a reduction process. When the potential is increased to −0.45 V (vs RHE), these Raman-active modes attributed to the spinel structure disappear, whereas a new peak assigned to the rock salt structure ($Co_yNi_{1-y}O$) at 532 cm^{-1} arises and remains with a further increase in potential. (38,40) These findings reconfirm that the $Co_{3-x}Ni_xO_4$ on the surface of the polyhedron is transformed *in situ* into $Co_yNi_{1-y}O$ during the electrochemical reduction, which acts as the real HER active species. Additionally, the microstructure of $Co_{3-x}Ni_xO_4$ crystals at different stages of chronoamperometry activation (at −0.18 V vs RHE) demonstrates the dynamic reconstruction process (Figure S5).

The electrocatalytic HER performance of the as-prepared electrodes was evaluated in 1 M KOH solution. As revealed in the linear scan voltammetry (LSV) polarization curves (Figure 3a), EA-$Co_{3-x}Ni_xO_4$/NF displays an overpotential of 57 mV at −10 mA cm^{-2}, which is substantially better than those of NF (259 mV) and $Co_{3-x}Ni_xO_4$/NF (114 mV) and is even close to that of the state of the art Pt/C catalyst (24 mV). Notably, although numerous electrocatalysts, especially those obtained by electrochemical reduction, are stable and highly active under working conditions, dramatic deactivation will occur when they experience oxidation in air or power outages. (27,41) However, for EA-$Co_{3-x}Ni_xO_4$/NF, after exposure to air for 48 h, the decay of HER activity is negligible (Figure S6), indicating the excellent chemical stability of $Co_yNi_{1-y}O$ on the surface of EA-$Co_{3-x}Ni_xO_4$. EA-$Co_{3-x}Ni_xO_4$/NF displays a Tafel slope of 76.9 mV dec^{-1}, much smaller than that of $Co_{3-x}Ni_xO_4$/NF (131.6 mV dec^{-1}), suggesting fast HER kinetics for EA-$Co_{3-x}Ni_xO_4$/NF (Figure 3b). Electrochemical impedance spectroscopy (EIS) of EA-$Co_{3-x}Ni_xO_4$/NF shows a smaller charge transfer resistance (R_{ct}) of 1.5 Ω in comparison to that of $Co_{3-x}Ni_xO_4$/NF (3.4 Ω), proving the enhanced charge transfer kinetics in the HER for EA-$Co_{3-x}Ni_xO_4$/NF (Figure 3c). By virtue of the cyclic voltammetry (CV) curves at different scan rates (Figure S7), the double-layer capacitance (C_{dl}) of EA-$Co_{3-x}Ni_xO_4$/NF is calculated to be 51.1 mF cm^{-2}, ~5 times greater than that of $Co_{3-x}Ni_xO_4$/NF, implying a high

exposure of the active sites (Figure 3d). The durability of EA-Co$_{3-x}$Ni$_x$O$_4$/NF probed by chronopotentiometry (CP) and chronoamperometry (CA) measurements is shown in Figure 3e. At a constant current density of −20 mA cm^{-2}, the overpotential shows a slight increase (~12 mV) over a period of 300 h, and the current density of the HER at −0.12 V (vs RHE) loses only ~6.2% relative to the initial value after the 300 h test. After such long-term electrocatalysis, the SEM image displays an unchanged morphology where numerous polyhedral crystals are still covered on the NF support without apparent exfoliation, indicating a tight combination between EA-Co$_{3-x}$Ni$_x$O$_4$ and the NF substrate (Figure 4a). Moreover, a TEM image reveals the loose surface of EA-Co$_{3-x}$Ni$_x$O$_4$ that is still composed of abundant nanoparticles, and the interplanar spacings of 0.21 and 0.24 nm can be well assigned to the (200) and (111) planes of cubic NiO (JCPDS 65-2901) or CoO (JCPDS 65-2902), respectively, suggesting a retained microstructure after the durability test (Figure 4b,c). Furthermore, there is no obvious change in the high-resolution Co 2p and Ni 2p spectra of EA-Co$_{3-x}$Ni$_x$O$_4$/NF after the 300 h CA test, which still consist of Co^{2+}/Co^{3+} and Ni^{2+}/Ni^{3+} where the high-valence metal ions (Co^{3+}/Ni^{3+}) are attributed to the surface oxidation of the catalyst exposed to the air (Figure 4d–f). (42,43)
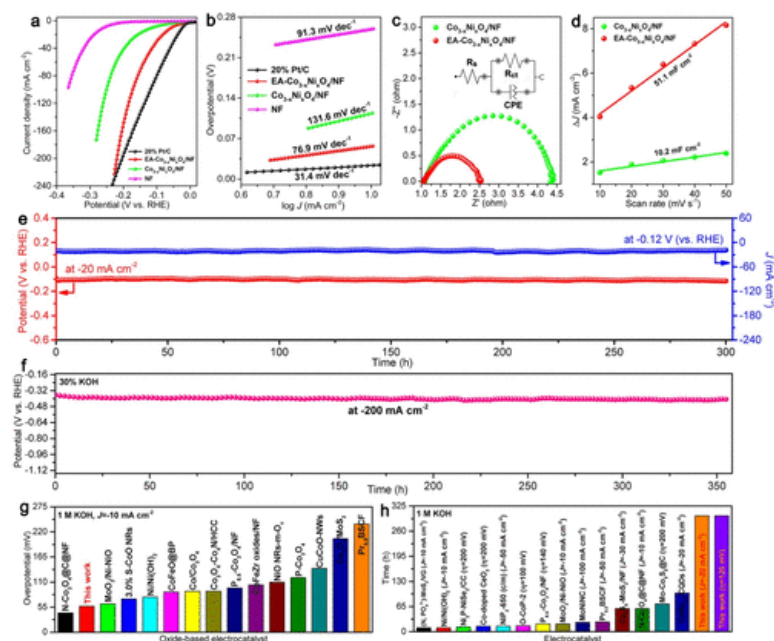
Figure 3. (a) *iR*-corrected LSV curves and (b) Tafel plots of Co$_{3-x}$Ni$_x$O$_4$/NF, EA-Co$_{3-x}$Ni$_x$O$_4$/NF, 20% Pt/C, and NF. (c) EIS of Co$_{3-x}$Ni$_x$O$_4$/NF and EA-Co$_{3-x}$Ni$_x$O$_4$/NF. Inset: equivalent circuit. (d) C_{dl} curves of Co$_{3-x}$Ni$_x$O$_4$/NF and EA-Co$_{3-x}$Ni$_x$O$_4$/NF. (e) CP test at a constant current density of −20 mA cm^{-2} and CA test at a fixed potential of −0.12 V (vs RHE) for EA-Co$_{3-x}$Ni$_x$O$_4$/NF in 1 M KOH solution. (f) CP test in 30 wt % KOH solution at a constant current density of −200 mA cm^{-2} (without *iR* correction). (g) Overpotential at −10 mA cm^{-2} of EA-Co$_{3-x}$Ni$_x$O$_4$/NF, in comparison with the values of representative oxide-based electrocatalysts. (h) Comparison of the HER stability of EA-Co$_{3-x}$N$_x$O$_4$/NF with other non-noble-metal-based electrocatalysts in 1 M KOH.
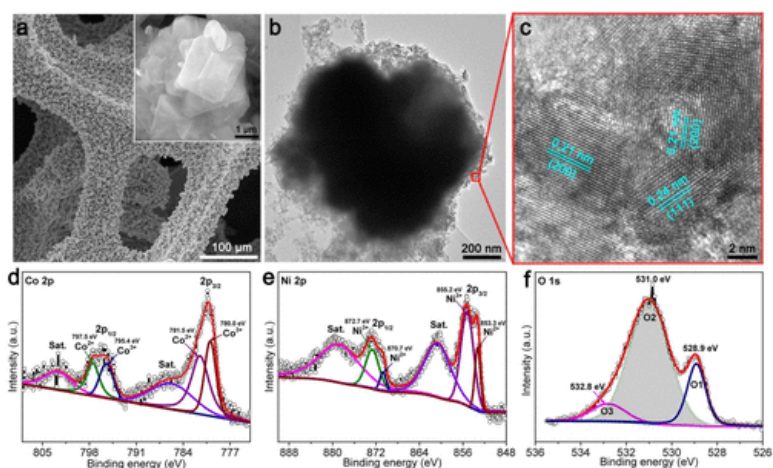
Figure 4. (a) SEM, (b) TEM, and (c) HRTEM images of EA-Co$_{3-x}$Ni$_x$O$_4$/NF after a 300 h CA test. High-resolution XPS spectra of (d) Co 2p, (e) Ni 2p, and (f) O 1s for EA-Co$_{3-x}$Ni$_x$O$_4$/NF after a 300 h CA test.

Since the industrial alkaline water electrolysis is often carried out in 30 wt % KOH solution, (44) we thus evaluated the HER performance of EA-Co$_{3-x}$Ni$_x$O$_4$/NF in a realistic 30 wt % KOH solution. As shown in Figure 3f, at a large current density of −200 mA cm^{-2}, EA-Co$_{3-x}$Ni$_x$O$_4$/NF can retain its electrocatalytic activity unchanged for more than 350 h. This result not only reconfirms the extraordinary structural and catalytic stability of the material for the HER but also demonstrates that the catalytic activity of EA-Co$_{3-x}$Ni$_x$O$_4$/NF meets the requirement in practical water-splitting technology. Additionally, it is worth noting that the activity and stability of EA-Co$_{3-x}$Ni$_x$O$_4$/NF are higher than those of most of the reported oxide-based and other non-noble-metal-based HER electrocatalysts in alkaline media (Figure 3g,h and Tables S1–S3). Inspired by the excellent HER performance, a full electrolyzer is assembled using EA-Co$_{3-x}$Ni$_x$O$_4$/NF as cathode and NiFe hydroxide/NF as anode. The as-prepared NiFe hydroxide/NF with a uniform nanosheet morphology requires an overpotential of 210 mV at 10 mA cm^{-2} for anodic water oxidation (Figure S8). The optical photograph and a video taken during the operation suggest that the electrolyzer can operate stably with rapid gas evolution (inset in Figure S9b and Movie S1). A cell voltage of only 1.52 V is needed to reach a current density of 10 mA cm^{-2} (Figure S9a), which outperforms most of the recently reported electrolyzers (Table S4). Additionally, the cell voltage shows a slight increment for the 128 h CP test at a constant current density of 20 mA cm^{-2} (Figure S9b), further suggesting the potential application of this noble-metal-free EA-Co$_{3-x}$Ni$_x$O$_4$/NF electrode in a practical water-splitting system.

DFT calculations have been further carried out to investigate the effects of surface structure (Ni$_y$Co$_{1-y}$O) on the catalytic properties of EA-Co$_{3-x}$Ni$_x$O$_4$ at an atomic level (Figures S10–S13). On the basis of the Tafel slope of EA-Co$_{3-x}$Ni$_x$O$_4$/NF, the HER pathway should follow the Volmer–Heyrovsky process: i.e. H$_2$O + e$^-$ → H$_{ad}$ + OH$_{ad}$ and OH$_{ad}$ + e$^-$ → OH$^-$ (Volmer step) and H$_2$O + e$^-$ + H$_{ad}$ → H$_2$ + OH$^-$ (Heyrovsky step). (45,46) The Volmer reaction is critical, but there has been very little research on the kinetics of OH$_{ad}$ + e$^-$ → OH$^-$. (46) As depicted in Figure 5a, DFT calculations indicate that the dissociated H$_{ad}$ and OH$_{ad}$ occupy the top sites (O site) and bridge sites (Ni–Ni, Co–Co, or Ni–Co site), respectively. According to the free energy diagram (Figure 5b and Tables S5 and S6), the Gibbs free energy change for the reaction H$_2$O + e$^-$ → H$_{ad}$ + OH$_{ad}$ is −1.404 eV (NiO), −3.098 eV (CoO), −1.041 eV (Ni-doped CoO) and −1.557 eV (Co-doped NiO), respectively. Hence, from a thermodynamic aspect, these models are beneficial for the water dissociation into H$_{ad}$ and OH$_{ad}$, in line with previous literature. (47) Additionally, the Gibbs free energy change between (H–OH)* and H* calculated from the free energy diagram is 1.290 eV (NiO), 3.055 eV (CoO), 0.870 eV (Ni-doped CoO), and 0.802 eV (Co-doped NiO), respectively. Obviously, Ni-doped CoO and Co-doped NiO are more likely to overcome the energy barrier and smoothly complete the desorption of OH$_{ad}$, thus promoting the kinetics of OH$_{ad}$ + e$^-$ → OH$^-$. In contrast, it is easy to cause the inefficient release of OH$_{ad}$ and poison the active sites due to the high desorption barrier of

OH$_{ad}$ on the surface of NiO and CoO. Moreover, the calculated OH$^-$ adsorption energies for NiO (-1.674 eV), CoO (-3.388 eV), Ni-doped CoO (-1.256 eV), and Co-doped NiO (-1.133 eV) also indicate that introducing Ni (or Co) atoms in the basal plane of CoO (or NiO) could facilitate the desorption of OH$_{ad}$ (Figure S14). Beyond that, the free energy of hydrogen adsorption (G_{H*}) is another crucial descriptor to evaluate the alkaline HER activity. The optimum value of G_{H*} is 0 eV, which means that hydrogen is bound to catalysts appropriately. (47) As shown in Figure 5b, G_{H*} values for the surfaces of CoO, NiO, and Ni-doped CoO are less negative and closer to the optimal value, suggesting that the combination of H$_{ad}$ to form H$_2$ is easy. This result can be also demonstrated from an adsorption energy diagram (Figure S14). According to Sabatier's principle, the optimal catalyst should bind the reactants "just right": i.e., neither too strong nor too weak. Therefore, on consideration of the adsorption/desorption equilibrium of H$_{ad}$ and OH$_{ad}$ involved in the alkaline HER, Ni-doped CoO is the most favorable among the four models.
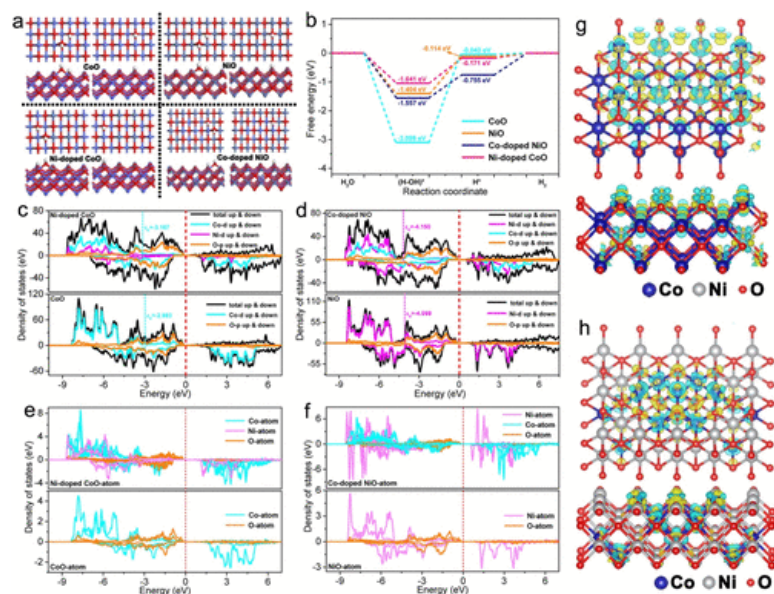
Figure 5. (a) Atomic configurations involved in the HER and (b) the corresponding free energy diagram for the HER on the surfaces of CoO (110), NiO (110), Ni-doped CoO (110), and Co-doped NiO (110). (c) PDOS of CoO (110) and Ni-doped CoO (110). (d) PDOS of NiO (110) and Co-doped NiO (110). (e) The DOS of each atom in CoO and Ni-doped CoO. (f) The DOS of each atom in NiO and Co-doped NiO. The charge density difference of (g) Ni-doped CoO and (h) Co-doped NiO. Yellow and cyan represent electron accumulation and electron depletion, respectively.

The density of state (DOS) is utilized to gain more insight into the difference in electronic structures among the four models. For the bulk phase of CoO and NiO, two equivalent energy states (spin-up and spin-down) can be found, implying their antiferromagnetism (Figure S15). The projected DOS (PDOS) results reveal that the d-band centers (ε_d) of surface metal sites in NiO, CoO, Co-doped NiO, and Ni-doped CoO are -4.098, -2.983, -4.190, and -3.167 eV, respectively, which clearly illustrates the ε_d value of Ni (or Co) in Co-doped NiO (or Ni-doped CoO) shifts to low energy relative to NiO (or CoO) (Figure 5c,d). The results also suggest that the antibonding energy states are lowered and the interaction between adsorbate and surface is weakened, (48) which is responsible for the decreasing binding strength of OH$_{ad}$ on the surface of Ni-doped CoO and Co-doped NiO. Moreover, in order to further analyze the DOS distribution, we calculated the DOS of each atom in the four models (Figure 5e,f). When they are taken together, because the d orbitals of each Ni (or Co) atom remain consistent in the NiO (or CoO) model, the DOSs of these Ni (or Co) atoms are coincident. However, after Co (or Ni) doping, the DOSs of each atom become inconsistent, indicating the rearrangement of electrons. The band gap of Co-doped NiO (or Ni-doped CoO) is narrower than that of NiO (or CoO), implying an improved electrical conductivity.

Moreover, it is worth noting that the DOS distribution of all the doped Ni atoms is consistent in Ni-doped CoO (Figure 5e). In contrast, the DOS distribution of all the doped Co atoms is inconsistent (Figure 5f), which leads to the strong orbital hybridization among Co, Ni, and O atoms. The stronger orbital hybridization will rearrange the electrons of O atoms. Furthermore, the difference charge density can directly reflect the change in charge density in the substrate material (NiO or CoO) after Co or Ni doping. As shown in Figure 5h, the enriched charge density around O atoms can be observed, which means an increased transition probability of wave function between O atoms and H_{ad}, thus suggesting an enhanced hydrogen adsorption ability. Meanwhile, the decreased charge density around the Co atoms in Co-doped NiO indicates the reduced adsorption ability toward OH_{ad}. Similarly, after doping Ni atoms in CoO, the charge depletion around the Ni atoms proves that Ni-doped CoO is also beneficial to the desorption of OH_{ad}, whereas the charge density of O atoms is relatively balanced, demonstrating that Ni doping has little effect on the hydrogen adsorption ability of CoO (Figure 5g). Overall, the calculation results exhibit that tailoring CoO with Ni not only optimizes the electrical conductivity but also promotes the desorption of OH_{ad} while ensuring a proper hydrogen adsorption energy, thus effectively accelerating the kinetics of $OH_{ad} + e^- \rightarrow OH^-$ and the overall kinetics of the alkaline HER. Therefore, we can conclude that Ni-doped CoO on the surface of EA-$Co_{3-x}Ni_xO_4$ plays a major role during the alkaline HER.

Conclusions

In summary, highly efficient EA-$Co_{3-x}Ni_xO_4$ electrocatalysts have been synthesized by *in situ* electrochemical activation of $Co_{3-x}Ni_xO_4$. The obtained EA-$Co_{3-x}Ni_xO_4$ exhibited favorable HER activity in alkaline medium with an overpotential of 57 mV at −10 mA cm^{-2} and remarkable stability (>300 h), which is superior to most of the reported electrocatalysts. In contrast to previous reports, the HER activity of EA-$Co_{3-x}Ni_xO_4$ shows negligible deterioration when it is exposed to air for 48 h. Systematic characterization demonstrated that the surface of EA-$Co_{3-x}Ni_xO_4$ is covered by intertwined $Co_yNi_{1-y}O$ nanoparticles (mixture of Ni-doped CoO and Co-doped NiO) as the catalytically active phase. The highly exposed {110} reactive facets in ultrafine $Co_yNi_{1-y}O$ can provide numerous active sites for the HER. DFT calculations further revealed that the Ni-doped CoO on the surface of EA-$Co_{3-x}Ni_xO_4$ can well tailor the electrical conductivity and the adsorption/desorption free energies of H_{ad} and OH_{ad} intermediates, thereby improving the kinetics of the alkaline HER. These findings not only unraveled the key active species for spinel Co_3O_4-based HER catalysts under alkaline conditions but also provided key insight into the rational design of high-efficiency HER electrocatalysts.

Supporting Information

The Supporting Information is available free of charge at https://pubs.acs.org/doi/10.1021/acscatal.1c01607.

- Experimental details, DFT calculations, SEM and TEM images, analysis of the dynamic reconstruction process, CA activation process, CV curves, polarization curves, water splitting test, structural models, diagram of adsorption energies, and DOS distribution (PDF)

- Rapid gas evolution of the electrolyzer (MP4)

Terms & Conditions

Notes

Acknowledgments

References

1 Rausch, B.; Symes, D. M.; Chisholm, G.; Cronin, L. Decoupled catalytic hydrogen evolution from a molecular metal oxide redox mediator in water splitting. *Science* **2014**, *345*, 1326– 1330, DOI: 10.1126/science.1257443

2 Zhu, J.; Hu, L.; Zhao, P.; Lee, L. Y. S.; Wong, K.-Y. Recent Advances in Electrocatalytic Hydrogen Evolution Using Nanoparticles. *Chem. Rev.* **2020**, *120*, 851– 918, DOI: 10.1021/acs.chemrev.9b00248

3 Subbaraman, R.; Tripkovic, D.; Strmcnik, D.; Chang, K.-C.; Uchimura, M.; Paulikas, A. P.; Vojislav, S.; Markovic, N. M. Enhancing Hydrogen Evolution Activity in Water Splitting by Tailoring Li^+-$Ni(OH)_2$-Pt Interfaces. *Science* **2011**, *334*, 1256– 1260, DOI: 10.1126/science.1211934

4 Yin, H.; Zhao, S.; Zhao, K.; Muqsit, A.; Tang, H.; Chang, L.; Zhao, H.; Gao, Y.; Tang, Z. Ultrathin platinum nanowires grown on single-layered nickel hydroxide with high hydrogen evolution activity. *Nat. Commun.* **2015**, *6*, 6430, DOI: 10.1038/ncomms7430

5 Yin, J.; Jin, J.; Zhang, H.; Lu, M.; Peng, Y.; Huang, B.; Xi, P.; Yan, C.-H. Atomic Arrangement in Metal-Doped NiS_2 Boosts the Hydrogen Evolution Reaction in Alkaline Media. *Angew. Chem., Int. Ed.* **2019**, *58*, 18676– 18682, DOI: 10.1002/anie.201911470

6 Hu, C.; Zhang, L.; Gong, J. Recent progress made in the mechanism comprehension and design of electrocatalysts for alkaline water splitting. *Energy Environ. Sci.* **2019**, *12*, 2620– 2645, DOI: 10.1039/C9EE01202H

7 McKone, J. R.; Sadtler, B. F.; Werlang, C. A.; Lewis, N. S.; Gray, H. B. Ni-Mo Nanopowders for Efficient Electrochemical Hydrogen Evolution. *ACS Catal.* **2013**, *3*, 166– 169, DOI: 10.1021/cs300691m

8 Vij, V.; Sultan, S.; Harzandi, A. M.; Meena, A.; Tiwari, J. N.; Lee, W.-G.; Yoon, T.; Kim, K. S. Nickel-Based Electrocatalysts for Energy-Related Applications: Oxygen Reduction, Oxygen Evolution, and Hydrogen Evolution Reactions. *ACS Catal.* **2017**, *7*, 7196– 7225, DOI: 10.1021/acscatal.7b01800

9 Shi, H.; Zhou, Y. T.; Yao, R. Q.; Wan, W. B.; Ge, X.; Zhang, W.; Wen, Z.; Lang, X. Y.; Zheng, W. T.; Jiang, Q. Spontaneously separated intermetallic Co_3Mo from nanoporous copper as versatile electrocatalysts for highly efficient water splitting. *Nat. Commun.* **2020**, *11*, 2940, DOI: 10.1038/s41467-020-16769-6

10 Liu, Y.; Li, X.; Zhang, Q.; Li, W.; Xie, Y.; Liu, H.; Shang, L.; Liu, Z.; Chen, Z.; Gu, L.; Tang, Z.; Zhang, T.; Lu, S. A General Route to Prepare Low-Ruthenium-Content Bimetallic Electrocatalysts for pH-Universal Hydrogen Evolution Reaction by Using Carbon Quantum Dots. *Angew. Chem., Int. Ed.* **2020**, *59*, 1718– 1726, DOI: 10.1002/anie.201913910

11 Song, H.; Li, Y.; Shang, L.; Tang, Z.; Zhang, T.; Lu, S. Designed controllable nitrogen-doped carbon-dots-loaded MoP nanoparticles for boosting hydrogen evolution reaction in alkaline medium. *Nano Energy* **2020**, *72*, 104730, DOI: 10.1016/j.nanoen.2020.104730

12 Yan, Y.; Lin, J.; Cao, J.; Guo, S.; Zheng, X.; Feng, J.; Qi, J. Activating and optimizing the activity of NiCoP nanosheets for electrocatalytic alkaline water splitting through the V doping effect enhanced by P vacancies. *J. Mater. Chem. A* **2019**, *7*, 24486, DOI: 10.1039/C9TA09283H

13 Yan, Y.; Bao, K.; Liu, T.; Cao, J.; Feng, J.; Qi, J. Minutes periodic wet chemistry engineering to turn bulk Co-Ni foam into hydroxide based nanosheets for efficient water decomposition. *Chem. Eng. J.* **2020**, *401*, 126092, DOI: 10.1016/j.cej.2020.126092

14 Yan, Y.; Wang, P.; Lin, J.; Cao, J.; Qi, J. Modification strategies on transition metal-based electrocatalysts for efficient water splitting. *J. Energy Chem.* **2021**, *58*, 446, DOI: 10.1016/j.jechem.2020.10.010

15 Zhu, Y.; Lin, Q.; Zhong, Y.; Tahini, H. A.; Shao, Z.; Wang, H. Metal oxide-based materials as an emerging family of hydrogen evolution electrocatalysts. *Energy Environ. Sci.* **2020**, *13*, 3361– 3392, DOI: 10.1039/D0EE02485F

16 Yang, L.; Zhou, H.; Qin, X.; Guo, X.; Cui, G.; Asiri, A. M.; Sun, X. Cathodic electrochemical activation of Co$_3$O$_4$ nanoarrays: a smart strategy to significantly boost the hydrogen evolution activity. *Chem. Commun.* **2018**, *54*, 2150– 2153, DOI: 10.1039/C7CC09416G

17 Cui, M.; Ding, X.; Huang, X.; Shen, Z.; Lee, T.-L.; Oropeza, F. E.; Hofmann, J. P.; Hensen, E. J. M.; Zhang, K. H. L. Ni^{3+}-Induced Hole States Enhance the Oxygen Evolution Reaction Activity of Ni$_x$Co$_{3-x}$O$_4$ Electrocatalysts. *Chem. Mater.* **2019**, *31*, 7618– 7625, DOI: 10.1021/acs.chemmater.9b02453

18 Liu, Z.; Wang, G.; Zhu, X.; Wang, Y.; Zou, Y.; Zang, S.; Wang, S. Optimal Geometrical Configuration of Cobalt Cations in Spinel Oxides to Promote Oxygen Evolution Reaction. *Angew. Chem., Int. Ed.* **2020**, *59*, 4736– 4742, DOI: 10.1002/anie.201914245

19 Zhu, Y. P.; Ma, T. Y.; Jaroniec, M.; Qiao, S. Z. Self-Templating Synthesis of Hollow Co$_3$O$_4$ Microtube Arrays for Highly Efficient Water Electrolysis. *Angew. Chem., Int. Ed.* **2017**, *56*, 1324– 1328, DOI: 10.1002/anie.201610413

20 Zhang, H.; Zhang, J.; Li, Y.; Jiang, H.; Jiang, H.; Li, C. Continuous oxygen vacancy engineering of the Co$_3$O$_4$ layer for an enhanced alkaline electrocatalytic hydrogen evolution reaction. *J. Mater. Chem. A* **2019**, *7*, 13506– 13510, DOI: 10.1039/C9TA03652K

21 Muthurasu, A.; Maruthapandian, V.; Kim, H. Y. Metal-organic framework derived Co$_3$O$_4$/MoS$_2$ heterostructure for efficient bifunctional electrocatalysts for oxygen evolution reaction and hydrogen evolution reaction. *Appl. Catal., B* **2019**, *248*, 202– 210, DOI: 10.1016/j.apcatb.2019.02.014

22 Liu, X.; Xi, W.; Li, C.; Li, X.; Shi, J.; Shen, Y.; He, J.; Zhang, L.; Xie, L.; Sun, X.; Wang, P.; Luo, J.; Liu, L.-M.; Ding, Y. Nanoporous Zn-doped Co$_3$O$_4$ sheets with single-unit-cell-wide lateral surfaces for efficient oxygen evolution and water splitting. *Nano Energy* **2018**, *44*, 371– 377, DOI: 10.1016/j.nanoen.2017.12.016

23 Liu, Y.; Liang, X.; Gu, L.; Zhang, Y.; Li, G.-D.; Zou, X.; Chen, J.-S. Corrosion engineering towards efficient oxygen evolution electrodes with stable catalytic activity for over 6000 h. *Nat. Commun.* **2018**, *9*, 2609, DOI: 10.1038/s41467-018-05019-5

24 Zhang, B.; Qin, H.; Diao, L.; Zhao, N.; Shi, C.; Liu, E.; He, C. Strongly coupled hollow-oxide/phosphide hybrid coated with nitrogen-doped carbon as highly efficient electrocatalysts in alkaline for hydrogen evolution reaction. *J. Catal.* **2019**, *377*, 582– 588, DOI: 10.1016/j.jcat.2019.08.007

25 Shang, X.; Dong, B.; Chai, Y.-M.; Liu, C.-G. In-situ electrochemical activation designed hybrid electrocatalysts for water electrolysis. *Sci. Bull.* **2018**, *63*, 853– 876, DOI: 10.1016/j.scib.2018.05.014

26 Zhai, L.; Benedict Lo, T. W.; Xu, Z.-L.; Potter, J.; Mo, J.; Guo, X.; Tang, C. C.; Edman Tsang, S. C.; Lau, S. P. In Situ Phase Transformation on Nickel-Based Selenides for Enhanced Hydrogen Evolution Reaction in Alkaline Medium. *ACS Energy Lett.* **2020**, *5*, 2483– 2491, DOI: 10.1021/acsenergylett.0c01385

27 Hu, C.; Ma, Q.; Hung, S.-F.; Chen, Z.-N.; Ou, D.; Ren, B.; Chen, H. M.; Fu, G.; Zheng, N. In Situ Electrochemical Production of Ultrathin Nickel Nanosheets for Hydrogen Evolution Electrocatalysis. *Chem.* **2017**, *3*, 122– 133, DOI: 10.1016/j.chempr.2017.05.011

28 Zou, X.; Wu, Y.; Liu, Y.; Liu, D.; Li, W.; Gu, L.; Liu, H.; Wang, P.; Sun, L.; Zhang, Y. In Situ Generation of Bifunctional, Efficient Fe-Based Catalysts from Mackinawite Iron Sulfide for Water Splitting. *Chem.* **2018**, *4*, 1139– 1152, DOI: 10.1016/j.chempr.2018.02.023

29 Wang, D.; Li, Q.; Han, C.; Lu, Q.; Xing, Z.; Yang, X. Atomic and electronic modulation of self-supported nickel-vanadium layered double hydroxide to accelerate water splitting kinetics. *Nat. Commun.* **2019**, *10*, 3899, DOI: 10.1038/s41467-019-11765-x

30 Zhao, Y.; Jia, X.; Chen, G.; Shang, L.; Waterhouse, G. I.N.; Wu, L.-Z.; Tung, C.-H.; O'Hare, D.; Zhang, T. Ultrafine NiO Nanosheets Stabilized by TiO$_2$ from Monolayer NiTi-LDH Precursors: An Active Water Oxidation Electrocatalyst. *J. Am. Chem. Soc.* **2016**, *138*, 6517– 6524, DOI: 10.1021/jacs.6b01606

31 Su, D.; Ford, M.; Wang, G. Mesoporous NiO crystals with dominantly exposed {110} reactive facets for ultrafast lithium storage. *Sci. Rep.* **2012**, *2*, 924, DOI: 10.1038/srep00924

32 Khassin, A. A.; Yurieva, T. M.; Kaichev, V. V.; Bukhtiyarov, V. I.; Budneva, A. A.; Paukshtis, E. A.; Parmon, V. N. Metal-support interactions in cobalt-aluminum co-precipitated catalysts: XPS and CO adsorption studies. *J. Mol. Catal. A: Chem.* **2001**, *175*, 189– 204, DOI: 10.1016/S1381-1169(01)00216-3

33 Bao, J.; Liu, W.; Xie, J.; Xu, L.; Guan, M.; Lei, F.; Zhao, Y.; Huang, Y.; Xia, J.; Li, H. $Ni_xCo_{3-x}O_4$ nanoneedle arrays grown on Ni foam as an efficient bifunctional electrocatalyst for full water splitting. *Chem. - Asian J.* **2019**, *14*, 480– 485, DOI: 10.1002/asia.201801710

34 Fominykh, K.; Feck, J. M.; Sicklinger, J.; Döblinger, M.; Böcklein, S.; Ziegler, J.; Peter, L.; Rathousky, J.; Scheidt, E.-W.; Bein, T.; Fattakhova-Rohlfing, D. Ultrasmall Dispersible Crystalline Nickel Oxide Nanoparticles as High-Performance Catalysts for Electrochemical Water Splitting. *Adv. Funct. Mater.* **2014**, *24*, 3123– 3129, DOI: 10.1002/adfm.201303600

35 Xia, C.; Jiang, Q.; Zhao, C.; Hedhili, M. N.; Alshareef, H. N. Selenide-Based Electrocatalysts and Scaffolds for Water Oxidation Applications. *Adv. Mater.* **2016**, *28*, 77– 85, DOI: 10.1002/adma.201503906

36 Yuan, C.; Li, J.; Hou, L.; Zhang, X.; Shen, L.; Lou, X. W. Ultrathin Mesoporous $NiCo_2O_4$ Nanosheets Supported on Ni Foam as Advanced Electrodes for Supercapacitors. *Adv. Funct. Mater.* **2012**, *22*, 4592– 4597, DOI: 10.1002/adfm.201200994

37 Dou, Y.; Liao, T.; Ma, Z.; Tian, D.; Liu, Q.; Xiao, F.; Sun, Z.; Ho Kim, J.; Dou, S. X. Graphene-like holey Co_3O_4 nanosheets as a highly efficient catalyst for oxygen evolution reaction. *Nano Energy* **2016**, *30*, 267– 275, DOI: 10.1016/j.nanoen.2016.10.020

38 Rivas-Murias, B.; Salgueiriño, V. Thermodynamic $CoO-Co_3O_4$ crossover using Raman spectroscopy in magnetic octahedron-shaped nanocrystals. *J. Raman Spectrosc.* **2017**, *48*, 837– 841, DOI: 10.1002/jrs.5129

39 Tong, X.; Xia, X.; Guo, C.; Zhang, Y.; Tu, J.; Fan, H. J.; Guo, X.-Y. Efficient oxygen reduction reaction using mesoporous Ni-doped Co_3O_4 nanowire array electrocatalysts. *J. Mater. Chem. A* **2015**, *3*, 18372– 18379, DOI: 10.1039/C5TA04593B

40 Li, X.; Dhanabalan, A.; Wang, C. Enhanced electrochemical performance of porous NiO-Ni nanocomposite anode for lithium ion batteries. *J. Power Sources* **2011**, *196*, 9625– 9630, DOI: 10.1016/j.jpowsour.2011.06.097

41 Ma, Q.; Hu, C.; Liu, K.; Hung, S.-F.; Ou, D.; Chen, H. M.; Fu, G.; Zheng, N. Identifying the electrocatalytic sites of nickel disulfide in alkaline hydrogen evolution reaction. *Nano Energy* **2017**, *41*, 148– 153, DOI: 10.1016/j.nanoen.2017.09.036

42 Fu, Q.; Wang, X.; Han, J.; Zhong, J.; Zhang, T.; Yao, T.; Xu, C.; Gao, T.; Xi, S.; Liang, C.; Xu, L.; Xu, P.; Song, B. Phase-Junction Electrocatalysts towards Enhanced Hydrogen Evolution Reaction in Alkaline Media. *Angew. Chem., Int. Ed.* **2020**, *59*, 259– 267, DOI: 10.1002/anie.202011318

43 Zhu, Y.; Chen, H.-C.; Hsu, C.-S.; Lin, T.-S.; Chang, C.-J.; Chang, S.-C.; Tsai, L.-D.; Chen, H. M. Operando Unraveling of the Structural and Chemical Stability of P-Substituted $CoSe_2$ Electrocatalysts toward Hydrogen and Oxygen Evolution Reactions in Alkaline Electrolyte. *ACS Energy Lett.* **2019**, *4*, 987– 994, DOI: 10.1021/acsenergylett.9b00382

44 Ju, W.; Heinz, M. V. F.; Pusterla, L.; Hofer, M.; Fumey, B.; Castiglioni, R.; Pagani, M.; Battaglia, C.; Vogt, U. F. Lab-Scale Alkaline Water Electrolyzer for Bridging Material Fundamentals with Realistic Operation. *ACS Sustainable Chem. Eng.* **2018**, *6*, 4829– 4837, DOI: 10.1021/acssuschemeng.7b04173

45 Wu, Y.; Liu, X.; Han, D.; Song, X.; Shi, L.; Song, Y.; Niu, S.; Xie, Y.; Cai, J.; Wu, S.; Kang, J.; Zhou, J.; Chen, Z.; Zheng, X.; Xiao, X.; Wang, G. Electron density modulation of $NiCo_2S_4$ nanowires by nitrogen incorporation for highly efficient hydrogen evolution catalysis. *Nat. Commun.* **2018**, *9*, 1425, DOI: 10.1038/s41467-018-03858-w

46 Mao, B.; Sun, P.; Jiang, Y.; Meng, T.; Guo, D.; Qin, J.; Cao, M. Identifying the Transfer Kinetics of Adsorbed Hydroxyl as a Descriptor of Alkaline Hydrogen Evolution Reaction. *Angew. Chem., Int. Ed.* **2020**, *59*, 15232– 15237, DOI: 10.1002/anie.202006722

47 Zhao, L.; Zhang, Y.; Zhao, Z.; Zhang, Q.-H.; Huang, L.-B.; Gu, L.; Lu, G.; Hu, J.-S.; Wan, L.-J. Steering elementary steps towards efficient alkaline hydrogen evolution via size-dependent Ni/NiO nanoscale heterosurfaces. *Natl. Sci. Rev.* **2020**, *7*, 27– 36, DOI: 10.1093/nsr/nwz145

48 Chen, Z.; Song, Y.; Cai, J.; Zheng, X.; Han, D.; Wu, Y.; Zang, Y.; Niu, S.; Liu, Y.; Zhu, J.; Liu, X.; Wang, G. Tailoring the d-Band Centers Enables Co_4N Nanosheets To Be Highly Active for Hydrogen Evolution Catalysis. *Angew. Chem., Int. Ed.* **2018**, *57*, 5076– 5080, DOI: 10.1002/anie.201801834